Volume 14 | Number 11 | 21 March 2018 | Pages 1967–2196

Soft Matter

rsc.li/soft-matter-journal

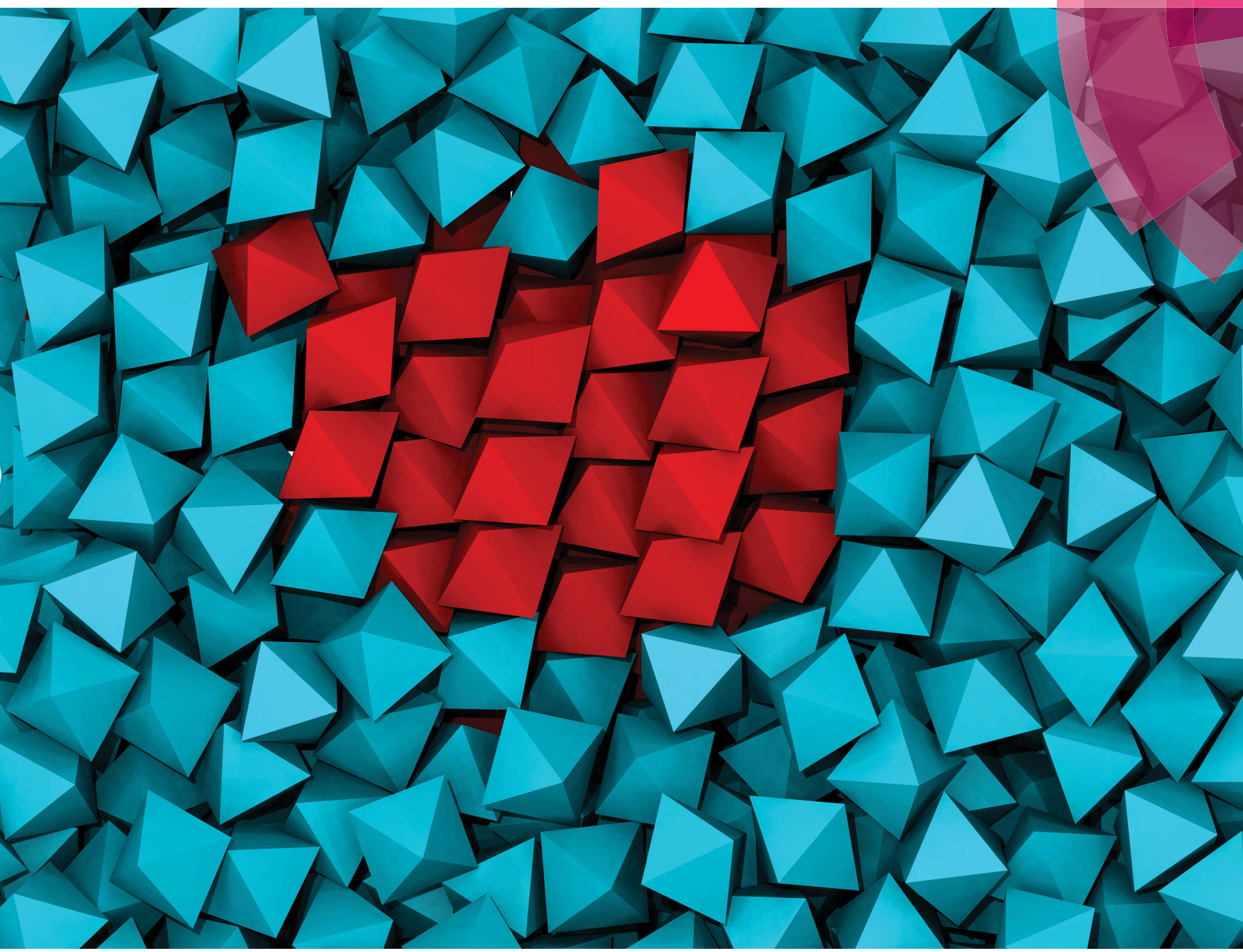

ISSN 1744-6848

ROYAL SOCIETY OF CHEMISTRY

PAPER

Fernando A. Escobedo *et al.*

Solid-phase nucleation free-energy barriers in truncated cubes: interplay of localized orientational order and facet alignment

Soft Matter

PAPER

View Article Online
View Journal | View Issue

Check for updates

Cite this: *Soft Matter*, 2018, **14**, 1996

Solid-phase nucleation free-energy barriers in truncated cubes: interplay of localized orientational order and facet alignment†

Abhishek K. Sharma,‡ Vikram Thapar‡ and Fernando A. Escobedo *

The nucleation of ordered phases from the bulk isotropic phase of octahedron-like particles has been studied *via* Monte Carlo simulations and umbrella sampling. In particular, selected shapes that form ordered (plastic) phases with various symmetries (cubic and tetragonal) are chosen to unveil trends in the free-energy barrier heights (ΔG^*'s) associated with disorder to order transitions. The shapes studied in this work have truncation parameter (s) values of 0.58, 0.75, 0.8 and 1. The case of octahedra (s = 1.0) is studied to provide a counter-example where the isotropic phase nucleates directly into a (Minkowski) crystal phase rather than a rotator phase. The simulated ΔG^*'s for these systems are compared with those previously reported for hard spheres and truncated cubes with s = 0.5 (cuboctahedra, CO) and s = 2/3 (truncated octahedra, TO). The comparison shows that, for comparable degrees of supersaturation, all rotator phases nucleate with smaller ΔG^*'s than that of the hard sphere crystal, whereas the octahedral crystal nucleates with a larger ΔG^*. Our analysis of near-critical translationally ordered nuclei of octahedra shows a strong bias towards an orientational alignment which is incompatible with the tendency to form facet-to-facet contacts in the disordered phase, thus creating an additional entropic penalty for crystallization. For rotator phases of octahedra-like particles, we observe that the strength of the localized orientational order correlates inversely with ΔG^*. We also observe that for $s > 0.66$ shapes and similar to octahedra, configurations with high facet alignment do not favor high orientational order, and thus ΔG^*'s increase with truncation.

Received 3rd December 2017,
Accepted 23rd January 2018

DOI: 10.1039/c7sm02377d

rsc.li/soft-matter-journal

Published on 23 January 2018. Downloaded by Cornell University Library on 11/6/2021 5:15:01 PM.

1 Introduction

Recent studies[1–10] have made remarkable progress in understanding the self-assembly of anisotropic particles. By virtue of their geometry, anisotropic particles have configurations that depend on the orientation of individual particles; *i.e.*, possess orientational degrees of freedom. Examples of experimentally synthesizable anisotropic particles include branched particles,[11,12] faceted polyhedra,[13–19] patterned particles,[20–23] and rod and ellipsoid shaped particles.[24–27] Among them, polyhedral particles are being extensively studied as they have well defined geometries that are amenable to both synthesis and modeling. Over the years, simulations have proven very useful in exploring the rich phase behavior of polyhedral particles of a diversity of shapes and for various extents of size polydispersity.[4–10] Using Monte Carlo simulations in the isothermal–isobaric ensemble, it was first shown[4] that some of the hard polyhedral particles that tessellate space undergo transitions from an disordered phase to a fully translationally and orientationally ordered phase *via* partially ordered phases termed "mesophases", which are defined as phases whose structural order is intermediate between disordered liquids and ordered crystals. Unlike spherical particles that form ordered phases having only translational order, the orientational degrees of freedom in anisotropic particles allow the formation of phases that may or may not be orientationally ordered. Thus, examples of mesophases of anisotropic particles include liquid crystals that are orientationally ordered but translationally disordered, and rotator plastic crystals that are translationally ordered but orientationally disordered.

One of the families of shapes that are readily synthesizable using a polyol process[17,18] is that of truncated cubes, defined by a truncation parameter, s, which varies from cubes (s = 0) *via* cuboctahedra (s = 0.5) to octahedra (s = 1). In this family, shapes with $s < 0.5$ are termed 'cube-like', while shapes with $s > 0.5$ are termed 'octahedron-like'. Recent computational studies[7,10] have rigorously examined the phase behavior of the truncated-cube family *via* simulation and revealed a rich diversity in crystal structures and plastic crystal mesophases. In particular, for octahedron-like particles, *i.e.*, shapes with $s > 0.5$, the

School of Chemical and Biomolecular Engineering, Cornell University, Ithaca, NY 14853, USA. E-mail: fe13@cornell.edu

† Electronic supplementary information (ESI) available. See DOI: 10.1039/c7sm02377d

‡ These authors contributed equally to this work.

This journal is © The Royal Society of Chemistry 2018

Published on 23 January 2018. Downloaded by Cornell University Library on 11/6/2021 5:15:01 PM.

lattice symmetry of the plastic mesophases transforms from body-centered tetragonal (BCT) to body-centered cubic (BCC) as the truncation is increased. This provides a simple illustration of how changes in faceting influences the stability of different lattice structures. Along with mapping the phase behavior, it would be interesting to explore how such changes in particle truncation and rotator lattice symmetry influence the kinetics of disorder-to-order phase transitions. Thapar and Escobedo[8] performed a computational study to explore the homogeneous nucleation kinetics from a disordered phase to a rotator phase of two shapes of the truncated cube family, namely, truncated octahedra (TO) (s = 2/3) and cuboctahedra (CO) (s = 0.5). It was shown that both these shapes nucleate the ordered phase more rapidly than hard spheres (HSs) at comparable degrees of supersaturation. It is unclear, however, whether other particle shapes in the same truncated cube family follow a similar trend or whether particular truncations are optimal in facilitating the nucleation of the solid phase.

The homogeneous nucleation of an ordered phase from an isotropic phase at small or moderate degrees of supersaturation is a rare event – it requires a critically large domain within the isotropic phase to seed a stable ordered nucleus. The unlikeliness of such a rare event makes its quantitative characterization using conventional brute force simulations computationally inefficient. Hence, many sophisticated sampling methods[28–39] have been developed to overcome this challenge. Among them, the umbrella sampling (US) method has been widely used to estimate the free energy barrier height associated with nucleation.[40,41] The technique involves biasing the system such that the rare events are sampled more frequently with a reasonable computational effort. The US calculations are performed along a reaction coordinate that tracks the progress of the nucleation process. Most crystal nucleation studies of hard particles have successfully employed the size of the largest solid like cluster[8,40–42] in the system as the reaction coordinate. Once the biased probabilities of forming clusters of different sizes are known, they are unbiased to obtain the free energy as a function of the reaction coordinate.

In this work, we apply US to estimate the nucleation barriers for the transition from a disordered phase to an ordered phase for hard octahedron-like ($s > 0.5$) particles. In particular, the shapes studied are octahedrons (Octs) and truncated cubes with truncation parameter s = 0.58 (TC58), s = 0.75 (TC75) and s = 0.8 (TC80). TC58, which is the truncated cube with minimum asphericity,[10] forms a plastic body-centered tetragonal (PBCT) lattice, while the other two form a body-centered cubic (PBCC) rotator phase. All three shapes undergo a first-order phase transition from an isotropic phase to a plastic crystal phase, whereas for Oct the system undergoes a phase transition from an isotropic phase to a Minkowski crystal phase.[7] To allow meaningful comparisons, we use US to simulate these transitions at comparable degrees of supersaturation, which quantifies the thermodynamic driving force to nucleation. For our comparisons, we will also peruse rotator-phase nucleation data for shapes with s = 0.5 (CO) and s = 2/3 (TO) from a previous simulation study.[8]

Our selection of methods and analysis is appropriate for the systems of interest as the phase transitions involved were well described by classical nucleation pathways. It should be noted, however, that non-classical pathways could also occur, especially for anisotropic particles,[4] where independent orientational and translational order may occur at different stages in the ordering process and lead to metastable or stable intermediary mesophases. This is important, for example, in isotropic-to-smectic phase transitions in hard rods[43] where two-step processes may occur with orientational order preceding translational order or *vice versa*. The occurrence of more complex ordering pathways is also well known in two-step freezing processes[44–48] where the particles form an intermediate dense liquid phase before translational order ensues. The existence of multistage mechanisms can be revealed by a detailed analysis of transition state configurations and transitional pathways.[8,40]

The rest of this paper is organized as follows. In Section 2 we describe the model used to simulate hard polyhedral particles, our choice of order parameter, and other relevant simulation details. In Section 3 we show and discuss our simulation results for nucleation free-energy barriers. Finally, in Section 4 we provide some concluding remarks.

2 Methods

2.1 Model

In this work, we use a hard particle pair potential given by:

$$\beta U_{ij} = \begin{cases} 0 & \text{if flag} = 1 \\ \infty & \text{if flag} = 0 \end{cases} \quad (1)$$

where U_{ij} is the interaction potential between particles i and j, and $\beta = 1/k_{\mathrm{B}}T$ (k_{B} is the Boltzmann constant and T is the temperature). The value of the variable flag is set to 1 if particles i and j do not overlap with each other, otherwise flag = 0. The overlapping of particle i with particle j is checked through the separating axis theorem[49] (which states that two convex shapes do not overlap, if there exists an axis on which their projections do not intersect).

2.2 Order parameters

For all the transitions studied in this work, the order parameter used is the number of particles in the largest translationally ordered cluster, n_{tr}. The crux in estimating this order parameter is to determine whether a given particle is "solid-like"; *i.e.*, translationally ordered. This is determined using the local bond order parameter analysis proposed by Steinhardt *et al.*[50] and used in several nucleation studies (*e.g.*, for hard spheres[40–42] and for TO and CO[8]). For every particle i, the local bond order parameter, $q_{l,m}(i)$, is defined by

$$q_{l,m}(i) = \frac{1}{N_{\mathrm{b}}(i)} \sum_{j=1}^{l} Y_{l,m}\left(\theta_{i,j}, \phi_{i,j}\right) \quad (2)$$

where $N_{\mathrm{b}}(i)$ is the number of neighbors of particle i, $Y_{l,m}(\theta,\phi)$ are the spherical harmonics, $\theta_{i,j}$ and $\phi_{i,j}$ are the polar and azimuthal angles between particle i and its neighbor j respectively, l is the symmetry index and the value of m ranges from $-l$ to l.

Published on 23 January 2018. Downloaded by Cornell University Library on 11/6/2021 5:15:01 PM.

In this work we use $l = 6$. The neighbors of particle i are those particles which are within the cutoff distance r_c of particle i; here we chose $r_c \approx 1.2$ times the distance to the first peak of the radial distribution function. The translational-order correlation between particle i and its neighbor j, $d_6(i,j)$ is given by:

$$d_6(i,j) = \frac{\sum_{m=-6}^{6} q_{6,m}(i) q_{6,m}^*(j)}{\sum_{m=-6}^{6} \left|\left(q_{6,m}(i)\right)^2\right|^{1/2} \left|\left(q_{6,m}(j)\right)^2\right|^{1/2}} \quad (3)$$

where the asterisk denotes the complex conjugate. Two particles i and j are defined as translationally connected if $d_6(i,j) > d_c$, which is the translational order correlation cutoff. In this case, we use a value of $d_c = 0.7$ as used in our earlier studies.[8] A particle with at least $\zeta_c = 7$ translational connections is classified as translationally ordered or solid-like. A solid-like cluster is identified using a criterion that if two solid like particles are within the cutoff distance, r_c, then they belong to the same cluster. This definition of the order parameter involves three tunable parameters: r_c, d_c, and ζ_c. In an earlier study,[41] it was demonstrated that umbrella sampling free-energy barrier calculations that used this definition of the order parameter are robust and relatively insensitive to variations of these tunable parameters. Consistent with such studies,[8,41] our preliminary tests also showed that while variations in such parameters altered the shape of the free energy landscape sampled (*e.g.*, the location of the critical nucleus size), the free energy difference between the transition state at the barrier top and the initial state remained largely unaffected.

As a complementary metric of order, for selected cases we also evaluated the global orientational order parameter, P_4, of the particles belonging to n_{tr}:

$$\begin{aligned} P_4 &= \max_n \frac{3}{14N} \sum_i P_4(\mathbf{u}_i \cdot \mathbf{n}) \\ &= \max_n \frac{3}{14N} \sum_i \left(35\cos^4 \tau_i(\mathbf{n}) - 30\cos^2 \tau_i(\mathbf{n}) + 3\right) \end{aligned} \quad (4)$$

where $\mathbf{u}_i$ is the unit vector along a relevant particle axis and $\mathbf{n}$ is a director unit vector which maximizes P_4 (see details in John *et al.*[51]). The summation is performed over all three axes for all n_{tr} particles in the nucleus. In this formulation of P_4, $P_4 = 1$ corresponds to perfect orientational order.

In order to study local orientational order, we use the I_4 orientational order parameter[52] that captures the relative orientation of a particle to an arbitrary reference coordinate frame. It uses spherical harmonics similar to q_6 but for angles associated with individual particle axis orientations instead of the bond orientation between two neighboring particles. In its normalized form it is evaluated for a given particle j as:

$$I_{4,m}(j) = \frac{\sum_{i=1}^{3} Y_{4,m}(\theta_i, \phi_i)}{\sqrt{\sum_{m=-4}^{4} \left|\sum_{i=1}^{3} Y_{4,m}(\theta_i, \phi_i)\right|^2}} \quad (5)$$

where $Y_{4,m}(\theta_i,\phi_i)$ are spherical harmonics with symmetry index 4, and θ_i and ϕ_i are the polar and azimuthal angles of the particles axis i to the reference coordinate frame. Analogous to d_6, the dot product in I_4 between two particles i and j is defined as:

$$d_4(i,j) = \sum_{m=-4}^{4} I_{4,m}(i) \cdot I_{4,m}^*(j) \quad (6)$$

where the asterisk (*) implies a complex conjugate. The two particles are assumed to be aligned if $d_4(i,j) > 0.7$. We use I_4 in conjunction with q_6 such that two neighboring particles are bonded if $d_4(i,j) > 0.7$ and $d_6(i,j) > 0.7$ simultaneously. Similar to q_6, a particle with at least 7 translational connections is termed solid-like, and if two solid like particles are within the cutoff distance, r_c, then they belong to the same cluster.

2.3 Facet alignment measure

It has been speculated in previous studies[19,53] that neighboring faceted particles might tend to align their facets in order to minimize their excluded volume and maximize their packing entropy. However, since calculation of the volume excluded by particles is a non-trivial, computationally intensive task, here we introduce a simpler surrogate metric that quantifies the extent of facet-to-facet matching, whose values are expected to correlate with the smallness of the excluded volume. Indeed, we exploit the fact that a signature of local efficient packing of particles is that the nearest facets tend to align parallel to each other, such that they would nearly completely overlap if viewed normal to one of the facets. Accordingly, we define a facet alignment measure, $\Delta(i,j)$, for any two neighboring particles i and j. In essence, it is the overlap area of the nearest facets (defined by the minimum centroid to centroid distance) when one is projected onto the other (Fig. 1). Since this operation can be performed in two different ways (*i.e.* projecting the facet from i onto the plane of the facet from j, and *vice versa*), the maximum of the two areas is taken to be the final value of $\Delta(i,j)$, thus making the operation commutative. The larger the value of Δ, the higher the facet alignment. $\Delta(i,j)$ is scaled with respect to the maximum possible value for a given system (*i.e.*, the area of the largest facet). In our calculations, neighboring particles were defined based on a Voronoi construction.[54] Since for any particle shape with facets of disparate sizes, the larger surface-area facets are expected to have a stronger tendency toward facet-to-facet alignment, for $s \geq 2/3$ only the hexagonal faces are considered for the nearest facet calculations.

It is important to note that Δ is in principle independent of local orientational order in that they need not be correlated, *i.e.*, there may be configurations with high facet-alignment but low orientational order and *vice versa*.

2.4 Simulation details

Metropolis Monte Carlo (MC) simulations were conducted in a cubic cell with periodic boundary conditions and $N = 2744$ particles. The simulations are performed at constant reduced pressure, $P^* = \beta P v$ (v is the volume of a shape), and constant temperature, T. Each MC cycle consisted of N translational

 This journal is © The Royal Society of Chemistry 2018

Published on 23 January 2018. Downloaded by Cornell University Library on 11/6/2021 5:15:01 PM.

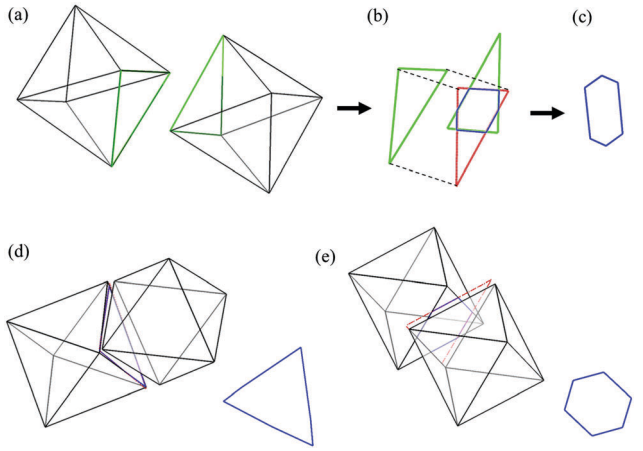

Fig. 1 Definition of the facet alignment measure, Δ, demonstrated for octahedra. (a) Nearest facets (green) are identified such that the centroid-to-centroid distance is the minimum. (b) One of the facets is projected (red) upon the plane of the other. The intersection of the projection with the other facet is obtained (blue). (c) The in-plane area of the intersection is calculated and normalized relative to the area of the triangular facet (the largest facet in the system). The calculation is repeated in the reverse order of facets and the higher value is taken. Sample configurations are shown for near-complete facet-to-facet alignment ($\Delta \sim 1$) in (d) and a staggered orientationally-ordered configuration present in the Minkowski crystal ($\Delta \sim 2/3$) in (e).

moves, N rotational moves, and one volume move. All trial moves are accepted according to the Metropolis criterion,[55] which requires ruling out overlaps between any two particles (*via* the separating axis theorem[49]). Each value of pressure, P^*, corresponds to a given value of degree of supersaturation (DSS), which is estimated *via*

$$\mathrm{DSS} = \beta|\Delta\mu| \tag{7}$$

where $\Delta\mu$ is the difference in chemical potential between the metastable liquid and the stable solid. $|\Delta\mu|$ represents the thermodynamic driving force for nucleating the new phase. The details for estimating DSS are provided in earlier publications.[8]

Since we focus on DSS conditions where brute force MC simulations are impractical to estimate the free energy barrier height to nucleation, ΔG^*, we employed umbrella sampling (US)[30,31] simulations to do so. US is performed by partitioning the phase space along the order parameter n_{tr} into a set of windows with overlapping boundaries. For each window, MC simulations are performed with rigid reflexive walls at the boundaries and keeping track of the number of times the system visits a given value of n_{tr}. While inside a given window, n_{tr} is allowed to change unbiased. To reduce computational costs, instead of evaluating the order parameters for every cycle,[40] we measure n_{tr} every 2 MC cycles. If the proposed move entails the change $n_{\mathrm{tr}}^{(\mathrm{o})} \rightarrow n_{\mathrm{tr}}^{(\mathrm{n})}$ and $n_{\mathrm{tr}}^{(\mathrm{n})}$ falls outside the window, the entire 2 MC cycle trajectory is rejected and the system is reset to the earlier configuration within the window which adds a visit to $n_{\mathrm{tr}}^{(\mathrm{o})}$. The histogram of visits $H(n_{\mathrm{tr}})$ thus collected is unbiased and it is directly used to estimate the free energies for each window *via* $\beta G(n_{\mathrm{tr}}) \sim -\ln H(n_{\mathrm{tr}})$ and the full free-energy profile is then obtained by matching the free-energy values obtained at the boundaries between consecutive windows; free energy values are shifted so that it is zero for $n_{\mathrm{tr}} = 0$ as a reference.

3 Results and discussion

3.1 Crystal nucleation of octahedrons (Octs)

To study the isotropic to crystal nucleation in Octs, US calculations were performed at various degrees of supersaturation using the largest q_6-based translationally ordered cluster as the reaction coordinate. The free energy barriers are tabulated in Table 1. Fig. 2 shows the free energy *versus* n_{tr} for DSS = 0.49, showing that free-energy barrier height, ΔG^*, is approximately $66.8k_{\mathrm{B}}T$.

Fig. 3 shows a comparison of nucleation barriers of isotropic to Minkowski crystal transitions in octahedrons with those for the isotropic to FCC crystal transition of HSs.[41] The comparison shows that the nucleation barriers for octahedrons are much larger than those of HSs for comparable DSS values. In order to understand why octahedra may have more difficulty ordering than HSs, we look for some clues in the microstructure of the near-critical nucleus. For this we collected and analyzed configurations from the US window near the top of the barrier (*i.e.*, for $180 < n_{\mathrm{tr}} < 200$ in Fig. 2). The orientation distribution function of the particles in these near-critical nuclei was obtained by plotting the components of all particle axes on

Table 1 Nucleation barriers for octahedra using umbrella sampling

Reduced pressure ($P^* = \beta p\sigma^3$)	Degree of supersaturation ($\beta\Delta\mu$)	Order parameter	Barrier height ($\beta\Delta G^*$)	Critical nucleus size
10.64	0.30	q_6	121.0	416
11.33	0.49	q_6	66.8	196
12.0	0.71	q_6	41.2	103
11.33	0.49	$q_6 \cap I_4$	68.2	172

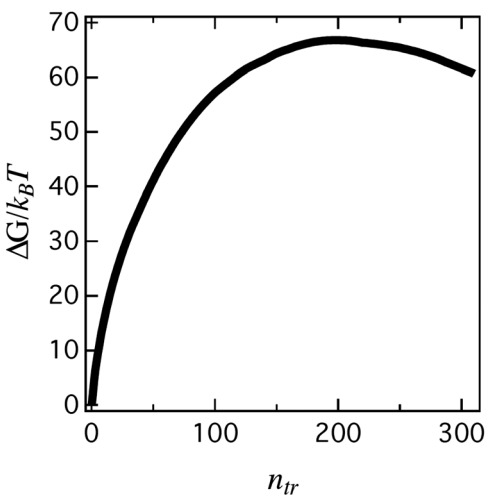

Fig. 2 Free-energy profile, $\Delta G/k_{\mathrm{B}}T$, *versus* n_{tr} obtained using US simulations for Octs at $P^* \approx 11.33$ (DSS = 0.49).

Published on 23 January 2018. Downloaded by Cornell University Library on 11/6/2021 5:15:01 PM.

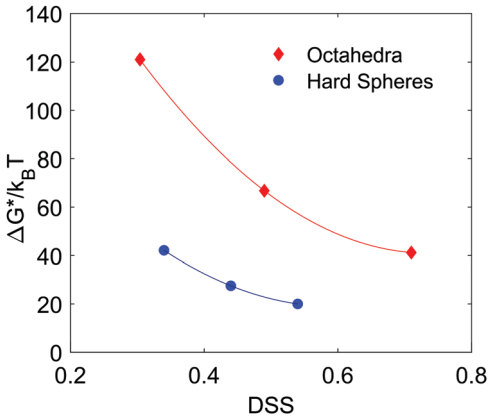

Fig. 3 Free-energy barrier-heights, $\Delta G^*/k_BT$, for octahedra and hard spheres[43] at different DSS values. Spline interpolations are shown as solid lines.

the surface of a unit sphere. As shown in Fig. 4(a), the particle orientation distribution clearly shows well-defined clusters at six different locations, indicative of preferential orientational alignment. This is further confirmed by the high value of global orientational order parameter $P_4 \approx 0.46$ for the particles in the nucleus. Although the order parameter n_{tr} is solely derived from translational correlations in a system, these results show that the particles in the nucleus tend to also pack with orientational alignment. To further validate the claim that orientational order is a characteristic feature of this transition, we performed the US simulation using a conjunction of q_6 and I_4 to define the ordered cluster to capture both orientational and translational order present (see the Methods section). The resulting nucleation barrier for $P^* = 11.33$ was still found to be higher than that of hard spheres and close to what was determined using q_6 alone (see Table 1). Thus, in contrast to the hard sphere case, orientational alignment is an essential feature of the crystalline nuclei in octahedra. Similar to the Minkowski crystal being nucleated, this orientational alignment has incomplete face-to-face alignment as seen in one of the snapshots of the portion of a $n_{tr} = 189$ nucleus shown in Fig. 4(b): the triangular faces are primarily staggered with respect to each other.

We now examine how local orientational order correlates with the facet-to-facet matching in the Minkowski crystal. For local orientational order we calculate d_4 from eqn (6) between neighboring particles. Parameter I_4 (see eqn 5) describes the preferential orientational alignment into six clusters of octahedral symmetry in Fig. 4(a). As shown in Fig. 4(c), d_4 captures the orientational alignment present in the Minkowski crystal in contrast to the disordered phase. Fig. 4(d) shows the variation in d_4 with respect to the facet alignment measure, Δ. It is evident that for $\Delta > 2/3$ increasing alignment correlates with a decrease in orientational alignment. Thus, the presence of configurations with neighboring particles aligning their facets in the isotropic phase hinders the orientational alignment needed to grow the Minkowski crystal. In order to nucleate into and grow the Minkowski crystal, the spontaneous orientational fluctuations in the isotropic phase must stir configurations away from complete face-to-face alignment. This additional restriction in the nucleation pathway reduces the probability of particles to assemble into the crystalline structure, hence increasing the free-energy barrier height for crystal nucleation in octahedra relative to hard spheres.

3.2 Rotator-phase nucleation of TC58, TC75 and TC80

In this section we compare the nucleation barriers for isotropic-to-plastic solid transition for particles with various degrees of truncations and degrees of supersaturation. For these comparisons, we group our results into shapes lying into two ranges: the first for $0.5 \leq s \leq 0.667$, and the second for $0.75 \leq s \leq 0.8$. The main reason for this grouping is that they correspond to shapes that form different types of rotator phase structures: the first group forms BCT-lattice, weakly-orientationally ordered rotators, while the second group forms a BCC-lattice, moderately-ordered rotator.[10] Fig. 5 and 6 and Table 2 show our results for $s = 0.58$, 0.75 and 0.8 as determined by US calculations using the largest q_6-based translationally ordered cluster as the reaction coordinate.

In order to compare nucleation free-energy barriers for shapes with different s for the same value of DSS = 0.34 (Fig. 6), we perform cubic spline interpolation for the data obtained here and other available data reported in previous studies[8] for cuboctahedra ($s = 0.5$) and truncated octahedra ($s = 2/3$). This particular value of DSS is chosen because it leads to barriers of the order of $\sim 20k_BT$, making them easier to estimate reliably *via* US (compared to very high or very small barriers which carry larger uncertainties) (Fig. 7).

In an earlier publication[8] we highlighted the role of orientational order in catalyzing the nucleation of rotator phases in anisotropic particles, including CO and TO. The degree of orientational order is reflected in the presence of certain preferred orientations in the rotator phase. As long as such preferred orientations are a subset of those orientations promoted by the natural tendency for facet-to-facet contacts between particles, the anisotropy of particle orientational distribution in the rotator phase can be seen as an indicator of the catalytic effect of local orientational order. As has been demonstrated,[10] all the rotator phases generated by particle shapes from the truncated cube family have a non-uniform orientational distribution and hence it is expected that the nucleation barriers for all cases considered here are lower than that observed for HSs.[40,41] However, the more diffuse (isotropic) the distribution of preferred orientations in the rotator phase is, the less the catalytic effect of orientational order is expected to be, because in the limit of particles approaching a fully isotropic orientational distribution, hard sphere like behavior would ensue.

We first examine the trends in ΔG^* data for the group of shapes in $0.5 \leq s \leq 0.667$. Shapes similar to TC58 undergo a first order phase transition from an isotropic to a rotator phase with a very small degree of global orientational order[10] (similar to that of the isotropic phase). In particular, for $s = 0.58$ the preferred orientations are spread over 18 clusters on the unit sphere and hence the nature of its isotropic–solid phase

 This journal is © The Royal Society of Chemistry 2018

Published on 23 January 2018. Downloaded by Cornell University Library on 11/6/2021 5:15:01 PM.

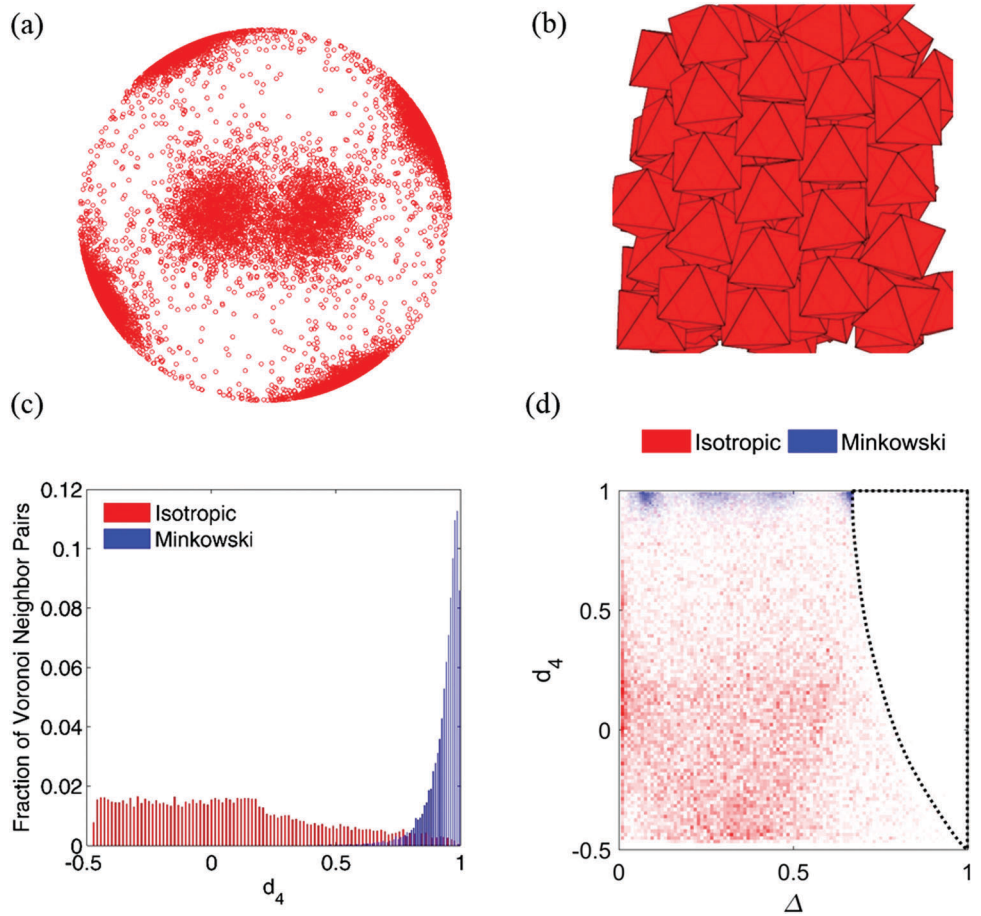

Fig. 4 Nucleation of the Minkowski crystal for octahedra at P^* = 11.33. (a) Particle orientation distribution function of near-critical nuclei with $180 < n_{tr} < 200$. The distribution is obtained over 20 different configurations. (b) Snapshot of a portion of the nucleus from one of these configurations with n_{tr} = 194. (c) Histogram of d_4 values for Voronoi neighbor pairs in a Minkowski crystal and the disordered phase. Both systems had 2744 particles. (d) 2D histogram plot of d_4 values for Voronoi neighbor pairs *vs.* the corresponding facet alignment measure values Δ (Δ = 1 implies perfect alignment). The darker the color the higher the number of neighbors belonging to that region. For $\Delta > 2/3$ possible orientational alignment is limited, the extent of which decreases with facet alignment, shown by the presence of a forbidden (empty) region on the top right of the plot (enclosed by dashed lines). Most particles in the crystal phase are restricted to $\Delta < 2/3$, as that is the maximum possible value of Δ for an orientationally aligned pair of particles, implying a staggered arrangement of the nearest triangular facets.

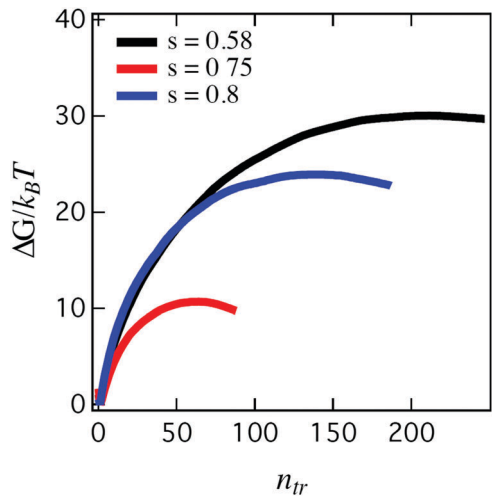

Fig. 5 Free-energy profiles, $\Delta G/k_BT$, *versus* n_{tr} obtained using US simulations for TC58, TC75 and TC80 for comparable DSSs ≈ 0.3, corresponding to P^* ≈ 7.60, 9.34 and 10.17, respectively.

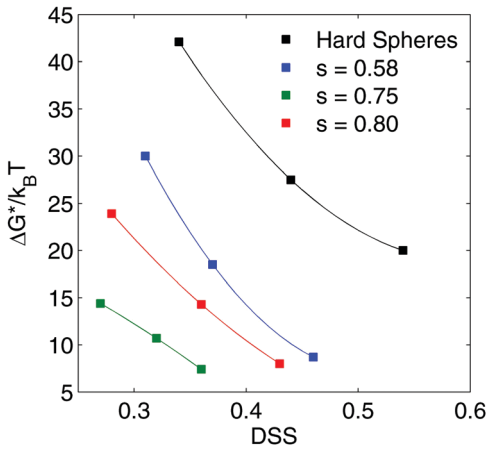

Fig. 6 Free-energy barrier-heights, $\Delta G^*/k_BT$, of TC58, TC75, TC80 and HSs[43] at different DSS values. Solid lines are cubic interpolations.

Published on 23 January 2018. Downloaded by Cornell University Library on 11/6/2021 5:15:01 PM.

Table 2 Nucleation barriers for truncated cubes using umbrella sampling. Error bars estimated from the uncertainties in the stitching of US windows and the determination of profile maximum

Truncation (s)	Degree of supersaturation ($\beta\Delta\mu$)	Barrier height ($\beta\Delta G^*$)	Critical nucleus size
0.58	0.31	30.0 ± 1.0	210
0.58	0.37	18.5 ± 0.5	140
0.58	0.46	8.7 ± 0.4	65
0.75	0.27	14.4 ± 0.4	85
0.75	0.32	10.7 ± 0.5	65
0.75	0.36	7.4 ± 0.4	40
0.8	0.28	23.9 ± 0.8	140
0.8	0.36	14.3 ± 0.6	80
0.8	0.43	8 ± 0.5	46

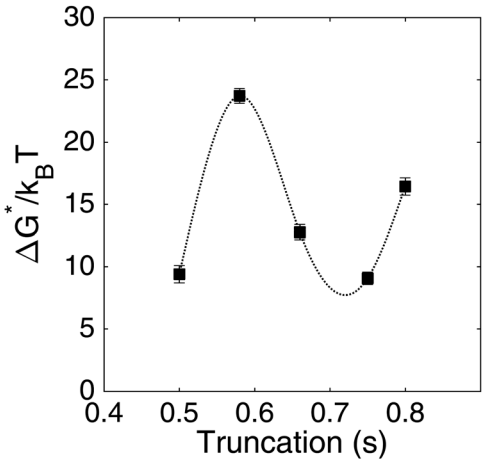

Fig. 7 Free-energy barrier-heights, $\Delta G^*/k_BT$, for isotropic to rotator phase transition for particle shapes with different truncations at DSS = 0.34. Data for CO and TO obtained from prior work.[8] For comparison, ΔG^* for HSs[41] at DSS = 0.34 would be $\sim 42 k_BT$.

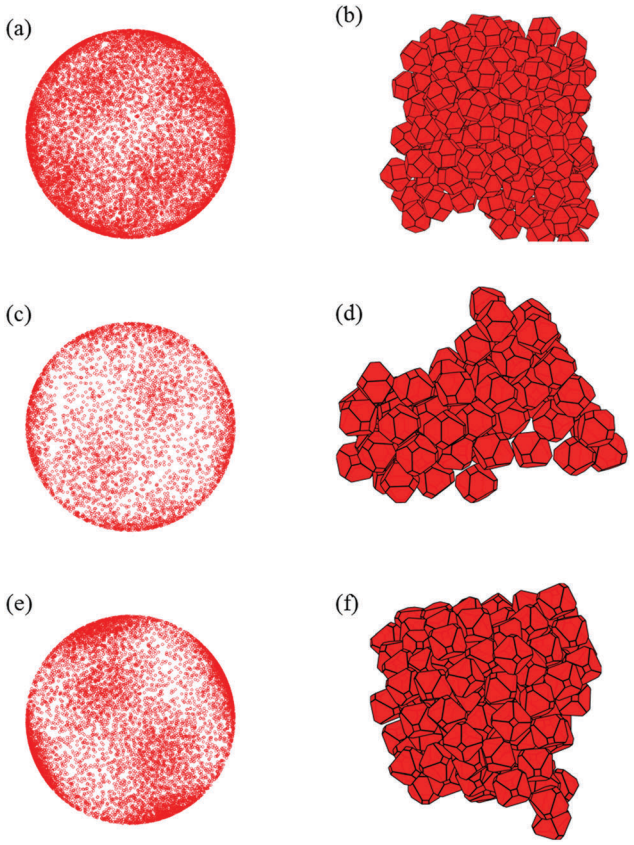

Fig. 8 Particle orientation distribution maps of near-critical nuclei for (a) TC58 at P^* = 7.60, (c) TC75 at P^* = 9.34 and (e) TC80 at P^* = 10.17. Each distribution is obtained over 20 different configurations. Snapshots of a portion of the nucleus are shown in (b) for TC58, (d) for TC75 and (f) for TC80.

transition would be close to that for HSs, where a globally translationally ordered and orientationally disordered phase is nucleated. This is further confirmed by plotting the particle orientation distribution of nuclei for $187 < n_{tr} < 217$ (near the top of the barrier for $P^* \approx 7.60$), which is seen in Fig. 8(a) to be quite diffuse, and by the small value of $P_4 \approx 0.07$ (the snapshot of a n_{tr} = 209 near-critical nucleus is shown in Fig. 8(b)). Such results are also consistent with the TC58 having the smallest asphericity among all shapes considered here.[10] In comparison, the critical nuclei of CO and TO have higher values for $P_4 \approx 0.1$ and 0.15 respectively (associated with 6 preferred clusters, the lower value in CO implying a more 'diffuse' clustering). Thus, it is expected that the catalytic effect of orientational order will be weaker in the case of TC58 and thus its nucleation barriers will be higher than those for CO and TO. Thus, the strength of the local orientational order correlates with lower nucleation barrier heights.

We now consider the second group of shapes with s = 0.75 and 0.80. The rotator phases of TC75 and TC80 are termed high-cubic plastic crystal phases,[10] as they have non-negligible global orientational order. Similar orientational order is also observed for nuclei near the top of the barrier for both TC75 and TC80, which is also related to that observed in the Minkowski lattice of perfect octahedra. As shown for TC75 at P^* = 9.34 and TC80 at P^* = 10.17 in Fig. 8(c) and (d), respectively, the orientation distributions of these nuclei show an inhomogeneous distribution with weak clustering in different regions, with TC75 exhibiting more scattered clusters compared to TC80. This clustering, however, is stronger than that of TO as indicated by the moderate P_4 values of 0.39 and 0.41 for TC75 and TC80 respectively. Snapshots of a portion of the near-critical nucleus for TC75 (n_{tr} = 62) and TC80 (n_{tr} = 148) are also shown in Fig. 8(d) and (f) respectively.

If we apply here the same criteria we used to explain trends in barrier heights for $s \in [0.5, 0.66]$, we would predict that the nucleation barriers for these shapes would be much lower than those of TO, with TC80 having a lower barrier than TC75. In contrast, we observe that TC80 has a higher free-energy barrier than TC75 for comparable DSSs. To understand this discrepancy, we must explore the spontaneous fluctuations in local order present in the isotropic phase and how they affect the nucleation behavior. Similar to the case with the Minkowski crystal in octahedra, we anticipate that a similar discord between facet-to-facet matching and orientational order might contribute to the increase of nucleation barriers. If we consider the distribution

This journal is © The Royal Society of Chemistry 2018

Published on 23 January 2018. Downloaded by Cornell University Library on 11/6/2021 5:15:01 PM.

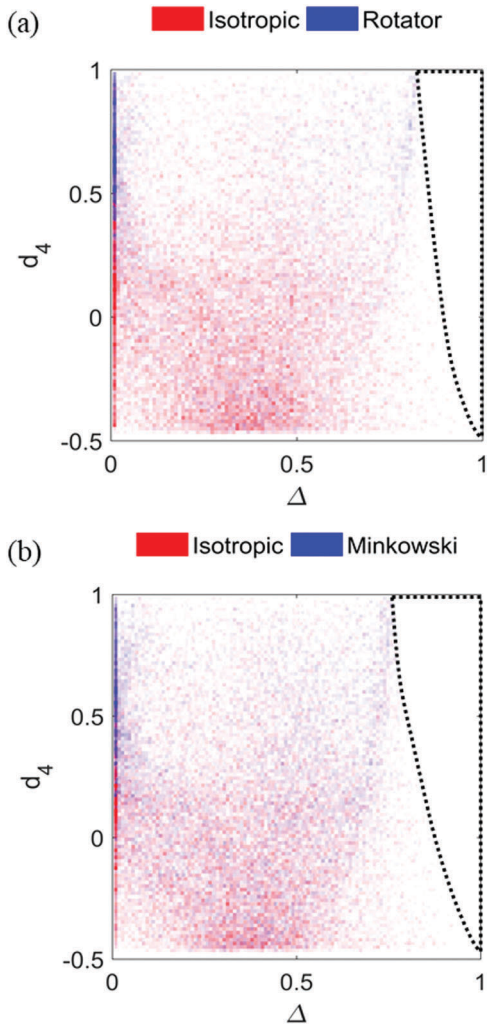

Fig. 9 2D histogram plots for d_4 values for Voronoi neighbor pairs *vs.* the corresponding facet alignment measure values (Δ) for (a) s = 0.75 and (b) s = 0.8, each for DSS $\approx$ 0.34. The systems contained 2744 particles. The darker the color the higher the number of neighbors belonging to that region. Similar to perfect octahedra, we observe that there is a 'forbidden' region (the empty area enclosed by dashed lines) on top right, which implies that high facet alignment can restrict orientational alignment. The size of the forbidden region is significantly larger for s = 0.8 in comparison to s = 0.75.

of facet alignment measures for both TC75 and TC80 (Fig. 9), we clearly observe that the size of the forbidden region on the top-right is larger for TC80. Moreover, due to a more scattered distribution of preferred orientations for TC75, more high-Δ configurations are explored by the particles in the rotator phase. Thus, the nucleation barrier is smaller for TC75 than for TC80 due to a reduced hindrance to nucleation pathways from states of high facet-to-facet matching. Using a similar line of reasoning, we predict a monotonous increase in the nucleation barrier for $s > 0.8$ as the lattice structure of the rotator phase essentially remains the same, while the hindrance associated with the forbidden region in the d_4–Δ diagram likely increases. As a limit, truncated octahedra (s = 0.66) do not have any significant forbidden region (see the ESI†).

4 Conclusion

In this work, we performed MC simulations to study the nucleation of ordered phases of selected octahedron-like shapes from the truncated cube family. The analysis unveils non-trivial trends in nucleation free energy barriers ΔG^* (as surrogates for describing nucleation kinetics) as a function of the extent of shape truncation. We demonstrate that for perfect octahedra the simulated nucleation barriers for nucleating the Minkowski crystal are much larger than those for solid-phase nucleation in HSs for comparable degrees of supersaturation. Our analysis of configurations of neighboring particles reveals that this transition to a crystal involves a mismatch between facet-to-facet alignment and local orientational order. Since facet-to-facet matching increases local packing entropy, configurations with high degrees of facet-to-facet alignment occur as spontaneous fluctuations in the isotropic phase, as quantified by a novel facet alignment metric. However, any two octahedra with near perfect facet matching will necessarily be orientationally misaligned, and are hence inconsistent with the high orientational order needed to realize the Minkowski crystal lattice. Since there is a spontaneous tendency for a subpopulation of particles in the isotropic phase to have such high facet alignment, such configurations hinder the nucleation pathways, resulting in higher values of ΔG^* as compared to systems where such hindrance is absent (like HSs).

It is the interplay between the tendency for facet alignment and local orientational order[8] among particles that underpins the attainment of translational-ordered packing and the observed trends in ΔG^* for particle shapes with varying degrees of truncation. In essence, local facet alignment may or may not be conducive to configurations that on average match the stable ordered structure, hence aiding or deterring the nucleation process. For all truncations (except for perfect octahedra which do not form a stable rotator phase), the estimated ΔG^* values for the isotropic-to-rotator phase transition are smaller than those for HSs at similar degrees of supersaturation, presumably due to the beneficial effect of local orientational order as described in earlier studies.[8] We also observe that such a catalytic effect of local orientational order correlates with the degree of overall orientational order in the incipient rotator phase (as detected, *e.g.*, by the clustering of particle orientations along preferential directions), which leads to a maximum for ΔG^* around TC58, whose critical nucleus has negligible orientational order. The near-isotropic particle orientation distribution in the solid nucleus of TC58 renders its ΔG^* values closer to those of HSs for comparable degrees of supersaturation. For $s > 0.66$, however, even as the local orientational order increases with increasing truncation, the rotator-nucleation barriers increase. In these cases, we infer that, instead of facilitating, facet alignment hinders some of the nucleation pathways that lead to the local orientational order required to form the solid phase (akin to the effect in octahedra), leading to higher barriers to nucleation as the truncation increases (and the octahedron shape is approached). Despite the complex interplay between orientational and translational order in the systems studied, we found no evidence for multi-step non-classical nucleation pathways.

Published on 23 January 2018. Downloaded by Cornell University Library on 11/6/2021 5:15:01 PM.

Future simulation studies could be aimed at calculating nucleation rates either by complementing ΔG^* data with the evaluation of kinetic prefactors[8,40,41] or by implementing transition path sampling methods.[37] In addition, to further test the hypotheses regarding the interplay between localized orientational order and facet alignment, similar analyses can be performed for other particle geometries. We anticipate that the effects of localized orientational order and facet-to-facet matching are general and can help in understanding the dynamics with which faceted particles self-assemble. However, the metrics we have used in this study are system specific and will require suitable extensions and specialization for application to systems with particles with different geometries/symmetries. Finally, the effect on the nucleation kinetics of shape and size polydispersity, a prevalent feature in experimental systems, should also be investigated. On the one hand, polydispersity may suppress some nucleation pathways as has been observed for hard spheres[56] (with large extent polydispersities eventually suppressing crystallization altogether[57,58]); on the other hand, in some systems a small degree of polydispersity could also lessen the facet-alignment-based hindrances that we have identified in this study.

This study adds to the body of work devoted to unveiling guidelines to engineer the self-assembly of anisotropic particles. Our analysis identifies some specific shapes that exhibit favorable kinetics for the homogeneous nucleation of translational order and the microscopic mechanisms that can be responsible for such behavior. For example, we have elucidated how local 2-particle correlations can aid or hinder collective phase transition phenomena. Such insights could be used to design fast self-assembling particles and external fields and additives that could act as catalysts for heterogeneous nucleation.

Conflicts of interest

There are no conflicts to declare.

Acknowledgements

Funding support from the NSF (award CBET-1402117) is gratefully acknowledged. This work used the Extreme Science and Engineering Discovery Environment (XSEDE), which was supported by the National Science Foundation (grant number ACI-1053575). The authors are also grateful to Unmukt Gupta for valuable exchanges.

References

1 G. M. Whitesides and M. Boncheva, *Proc. Natl. Acad. Sci. U. S. A.*, 2002, **99**, 4769–4774.
2 C. Burda, X. Chen, R. Narayanan and M. A. El-Sayed, *Chem. Rev.*, 2005, **105**, 1025–1102.
3 S. C. Glotzer and M. J. Solomon, *Nat. Mater.*, 2007, **6**, 557–562.
4 U. Agarwal and F. A. Escobedo, *Nat. Mater.*, 2011, **10**, 230–235.
5 P. F. Damasceno, M. Engel and S. C. Glotzer, *ACS Nano*, 2012, **6**, 609–614.
6 P. F. Damasceno, M. Engel and S. C. Glotzer, *Science*, 2012, **337**, 453–457.
7 A. P. Gantapara, J. De Graaf, R. Van Roij and M. Dijkstra, *Phys. Rev. Lett.*, 2013, **111**, 015501.
8 V. Thapar and F. A. Escobedo, *Phys. Rev. Lett.*, 2014, **112**, 048301.
9 M. R. Khadilkar and F. A. Escobedo, *Phys. Rev. Lett.*, 2014, **113**, 165504.
10 A. P. Gantapara, J. De Graaf, R. Van Roij and M. Dijkstra, *J. Chem. Phys.*, 2015, **142**, 54904.
11 L. Manna, D. J. Milliron, A. Meisel, E. C. Scher and A. P. Alivisatos, *Nat. Mater.*, 2003, **2**, 382–385.
12 S. Chen, Z. L. Wang, J. Ballato, S. H. Foulger and D. L. Carroll, *J. Am. Chem. Soc.*, 2003, **125**, 16186–16187.
13 Y. Sun and Y. Xia, *Science*, 2002, **298**, 2176–2179.
14 N. Malikova, I. Pastoriza-Santos, M. Schierhorn, N. A. Kotov and L. M. Liz-Marzán, *Langmuir*, 2002, **18**, 3694–3697.
15 K. S. Cho, D. V. Talapin, W. Gaschler and C. B. Murray, *J. Am. Chem. Soc.*, 2005, **127**, 7140–7147.
16 D. Dendukuri, D. C. Pregibon, J. Collins, T. A. Hatton and P. S. Doyle, *Nat. Mater.*, 2006, **5**, 365–369.
17 D. Seo, C. P. Ji and H. Song, *J. Am. Chem. Soc.*, 2006, **128**, 14863–14870.
18 O. C. Compton and F. E. Osterloh, *J. Am. Chem. Soc.*, 2007, **129**, 7793–7798.
19 J. Henzie, M. Grünwald, A. Widmer-Cooper, P. L. Geissler and P. Yang, *Nat. Mater.*, 2011, **11**, 131–137.
20 B. R. Martin, D. J. Dermody, B. D. Reiss, M. Fang, L. A. Lyon, M. J. Natan and T. E. Mallouk, *Adv. Mater.*, 1999, **11**, 1021–1025.
21 K.-H. Roh, D. C. Martin and J. Lahann, *Nat. Mater.*, 2005, **4**, 759–763.
22 G. Zhang, D. Wang and H. Möhwald, *Angew. Chem., Int. Ed.*, 2005, **44**, 7767–7770.
23 A. M. Jackson, Y. Hu, P. J. Silva and F. Stellacci, *J. Am. Chem. Soc.*, 2006, **128**, 11135–11149.
24 S.-S. Chang, C.-L. Lee and C. R. C. Wang, *J. Phys. Chem. B*, 1997, **101**, 6661–6664.
25 X. Peng, L. Manna, W. Yang, J. Wickham, E. Scher, A. Kadavanich and A. Alivisatos, *Nature*, 2000, **404**, 59–61.
26 F. M. van der Kooij, K. Kassapidou and H. N. W. Lekkerkerker, *Nature*, 2000, **406**, 868–871.
27 A. Mohraz and M. J. Solomon, *Langmuir*, 2005, **21**, 5298–5306.
28 R. J. Allen, P. B. Warren and P. R. Ten Wolde, *Phys. Rev. Lett.*, 2005, **94**, 18104.
29 R. J. Allen, D. Frenkel and P. R. Ten Wolde, *J. Chem. Phys.*, 2006, **124**, 194111.
30 S. L. Meadley and F. a Escobedo, *J. Chem. Phys.*, 2012, **137**, 74109.
31 G. M. Torrie and J. P. Valleau, *J. Comput. Phys.*, 1977, **23**, 187–199.
32 J. S. Van Duijneveldt and D. Frenkel, *J. Chem. Phys.*, 1992, **96**, 4655–4668.

 This journal is © The Royal Society of Chemistry 2018

Published on 23 January 2018. Downloaded by Cornell University Library on 11/6/2021 5:15:01 PM.

33 P. R. Ten Wolde, M. J. Ruiz-Montero and D. Frenkel, *Phys. Rev. Lett.*, 1995, **75**, 2714–2717.
34 P. Rein ten Wolde, M. J. Ruiz-Montero and D. Frenkel, *J. Chem. Phys.*, 1996, **104**, 9932–9947.
35 C. Dellago, P. G. Bolhuis, F. S. Csajka and D. Chandler, *J. Chem. Phys.*, 1998, **108**, 1964–1977.
36 C. Dellago, P. G. Bolhuis and D. Chandler, *J. Chem. Phys.*, 1999, **110**, 6617–6625.
37 T. S. van Erp, D. Moroni and P. G. Bolhuis, *J. Chem. Phys.*, 2003, **118**, 7762.
38 T. S. van Erp and P. G. Bolhuis, *J. Comput. Phys.*, 2005, **205**, 157–181.
39 B. Peters and B. L. Trout, *J. Chem. Phys.*, 2006, **125**, 54108.
40 S. Auer and D. Frenkel, *J. Chem. Phys.*, 2004, **120**, 3015–3029.
41 L. Filion, M. Hermes, R. Ni and M. Dijkstra, *J. Chem. Phys.*, 2010, **133**, 244115.
42 S. Auer and D. Frenkel, *Nature*, 2001, **409**, 1020–1023.
43 A. Cuetos, E. Sanz and M. Dijkstra, *Faraday Discuss.*, 2010, **144**, 253–269.
44 H. J. Schope, G. Bryant and W. Van Megen, *Phys. Rev. Lett.*, 2006, **96**, 175701.
45 J. Russo and H. Tanaka, *MRS Bull.*, 2016, **41**, 369–374.
46 S. Karthika, T. K. Radhakrishnan and P. Kalaichelvi, *Cryst. Growth Des.*, 2016, **16**, 6663–6681.
47 P. J. M. Smeets, A. R. Finney, W. J. E. M. Habraken, F. Nudelman, H. Friedrich, J. Laven, J. J. De Yoreo, P. M. Rodger and N. A. J. M. Sommerdijk, *Proc. Natl. Acad. Sci. U. S. A.*, 2017, 201700342.
48 J. F. Lutsko and G. Nicolis, *Phys. Rev. Lett.*, 2006, **96**, 046102.
49 S. Gottschalk, M. C. Lin and D. Manocha, *Proc. ACM Siggraph*, 1996, 171–180.
50 P. Steinhardt, D. Nelson and M. Ronchetti, *Phys. Rev. B: Condens. Matter Mater. Phys.*, 1983, **28**, 784–805.
51 B. S. John, C. Juhlin and F. A. Escobedo, *J. Chem. Phys.*, 2008, **128**, 44909.
52 F. A. Escobedo, *J. Chem. Phys.*, 2016, **145**, 211903.
53 G. van Anders, D. Klotsa, N. K. Ahmed, M. Engel and S. C. Glotzer, *Proc. Natl. Acad. Sci. U. S. A.*, 2014, **111**, E4812–E4821.
54 M. P. Allen and D. J. Tildesley, *Computer Simulation of Liquids*, 1987, vol. 18.
55 N. Metropolis, A. W. Rosenbluth, M. N. Rosenbluth, A. H. Teller and E. Teller, *J. Chem. Phys.*, 1953, **21**, 1087–1092.
56 S. Auer and D. Frenkel, *Nature*, 2001, **413**, 711–713.
57 U. Agarwal and F. A. Escobedo, *J. Chem. Phys.*, 2012, **137**, 024905.
58 F. A. Escobedo, *J. Chem. Phys.*, 2014, **140**, 094102.